Nanoscale Res Lett (2010) 5:550–558
DOI 10.1007/s11671-009-9520-6

SPECIAL ISSUE ARTICLE

Nano-regime Length Scales Extracted from the First Sharp Diffraction Peak in Non-crystalline SiO_2 and Related Materials: Device Applications

Gerald Lucovsky · James C. Phillips

Received: 11 September 2009 / Accepted: 17 December 2009 / Published online: 6 January 2010

Abstract This paper distinguishes between two different scales of medium range order, MRO, in non-crystalline SiO_2: (1) the first is ~0.4 to 0.5 nm and is obtained from the position of the first sharp diffraction peak, FSDP, in the X-ray diffraction structure factor, S(Q), and (2) the second is ~1 nm and is calculated from the FSDP full-width-at-half-maximum FWHM. Many-electron calculations yield Si–O third- and O–O fourth-nearest-neighbor bonding distances in the same 0.4–0.5 nm MRO regime. These derive from the availability of empty Si dπ orbitals for back-donation from occupied O pπ orbitals yielding narrow symmetry determined distributions of third neighbor Si–O, and fourth neighbor O–O distances. These are segments of six member rings contributing to connected six-member rings with ~1 nm length scale within the MRO regime. The unique properties of non-crystalline SiO_2 are explained by the encapsulation of six-member ring clusters by five- and seven-member rings on average in a compliant hard-soft nano-scaled inhomogeneous network. This network structure minimizes macroscopic strain, reducing intrinsic bonding defects as well as defect precursors. This inhomogeneous CRN is enabling for applications including thermally grown ~1.5 nm SiO_2 layers for Si field effect transistor devices to optical components with centimeter dimensions. There are qualitatively similar length scales in nano-crystalline HfO_2 and phase separated Hf silicates based on the primitive unit cell, rather than a ring structure. Hf oxide dielectrics have recently been used as replacement dielectrics for a new generation of Si and Si/Ge devices heralding a transition into nano-scale circuits and systems on a Si chip.

Keywords Non-crystalline materials · Nano-crystalline thin films · Nano-crystalline/non-crystalline composites · Chemical bonding self-organizations · Percolation theory

G. Lucovsky (✉)
Department of Physics, North Carolina State University, Raleigh, NC 27695-8202, USA
e-mail: lucovsky@ncsu.edu

J. C. Phillips
Department of Physics and Astronomy, Rutgers University, Piscataway, NJ 08854, USA

Introduction

There have been many models proposed for the unique properties of non-crystalline SiO_2. These are based on the concept of the continuous random network, CRN, structure as first proposed by Zachariasen [1, 2]. CRN models assume the short range order, SRO, of SiO_2 is comprised of fourfold coordinated Si in tetrahedral environments through corner-connected twofold coordinated O bridging two Si atoms in a bent geometry. The random character of the network has generally been attributed to a wide distribution of Si–O–Si bond angles, 150 ± 30° as determined by X-ray diffraction [3], as well as a random distribution of dihedral angles. These combine to give a distribution of ring geometries that defines a compliant and strain free CRN structure [2].

More recently, a semi-empirical bond constraint theory (SE-BCT) was proposed by one of the authors (JCP) to correlate the ease of glass formation in SiO_2 and chalcogenide glass with local bonding constraints associated with two-body bond-stretching and three-body bond-bending forces [4, 5]. The criterion for ease of glass formation was a mean-field relation equating the average number of stretching and bending constraints/atom with the network dimensionality of three. When applied to SiO_2, satisfaction of this criterion was met by assuming a broken bond

bending constraint for the bridging O-atoms. This was inferred from the large bond angle distribution of the Si–O–Si bonding group, and the weak bonding force constant. The same local mean-field approach for the ease of glass formation has been applied with good success to other non-crystalline network glasses in the Ge–Se and As–Se alloy systems.

SE-BCT makes no connection with medium MRO that is a priori deemed to be important with other properties. As such, SE-BCT cannot identify MRO bonding that has been associated with the FSDP [6, 7]. Based on these references, the position and width of the FSDP identify two different MRO length scales. It will be demonstrated in this paper that these length scales provide a basis for explaining some of the unique nano-scale related properties of non-crystalline SiO_2 that are enabling for device applications.

The FSDP in the structure factor, S(Q), has been determined from X-ray and neutron diffraction studies of oxide, silicate, germanate, borate and chalcogenide glasses [7]. There is a consensus that the position and width of this feature derive from MRO [6–8]. This is defined as order extending beyond the nearest- and next-nearest neighbor distances extracted from diffraction studies, and displayed in radial distribution function plots [2]. There has been much speculation and empirical modeling addressing the microscopic nature of bonding arrangements in the MRO regime including rings of bonded atoms [9], distances between layer-like ordering [10], and/or void clustering that are responsible for the FSDP [11]. First-principle molecular dynamics calculations have been applied to the FSDP [7, 12]. One of these papers ruled out models based on layer-like nano-structures, and nano-scale voids as the MRO responsible for the FSDP [12]. References [7] and [12] did not offered alternative explanations for the FSDP based a microscopic understanding of the relationship between atomic pair correlations in the MRO regime and constraints imposed by fundamental electronic structure at the atomic and molecular levels.

Moss and Price in [7], building on the 1974 deNeufville et al. [6] observation and interpretation of the FSDP proposed that the position this feature, $Q_1(\text{Å}^{-1})$, "can be related, via an approximate reciprocal relation, to a distance R in real space by the expression $R = 2\pi/Q$". It is important to note the MRO-scale bonding structures previously proposed in [9] and [10], and ruled out in [12], could not explain why a large number of oxide and chalcogenide glasses exhibit FSDP's in a relative narrow regime of Q-values, $\sim$1 to 1.6 Å^{-1}. Nor could they account for the systematic differences among these Q-values, $\sim$1.5 for oxides, and 1.0–1.25 for chalcogenides. It has been shown in [13] that this is a result of an scaling relationship between the position of the FSDP in Q-space and the nearest neighbor bond length.

Based on [7, 8, 13, 14], the position, $Q_1(\text{Å}^{-1})$, and full-width at half-maximum, FWHM, $\Delta Q_1(\text{Å}^{-1})$ of the FSDP have been used to identify a second length scale within the MRO regime for a representative set of oxide and chalcogenide glasses [7, 11]. The first length scale has been designated as a correlation length, $R = 2\pi/Q_1(\text{Å}^{-1})$, and is determined from the Q-space position of the spectral peak as suggested in [1], and the second has been designated as a coherence length, $L = 2\pi/\Delta Q_1(\text{Å}^{-1})$, and is determined from the FWHM [7]. This interpretation of the FSDP position and line-shape is consistent with the interpretation of diffraction peaks or local maxima in S(Q) for non-crystalline and crystalline solids [2]. These are interpreted as inter-atomic distances or equivalently atomic pair correlations that are repeated throughout a significant volume of the sample within the X-ray beam, but not in a periodic manner characteristic of long range crystalline order. Like other diffraction features, e.g., the width of the Si–Si pair correlation length in SiO_2 as determined in [3], is also associated with a characteristic real space distance, e.g., of a MRO-scale cluster of atoms.

In referring to the FSDP, Moss and Prince in [7] noted that "such a diffraction feature thus represents the build up of correlation whose basic period is well beyond the first few neighbor distances"; this basic period is within the MRO domain. It was also pointed out by them that "In fact, the width of this feature can be used to estimate a correlation range over which the period in question survives", or persists.

Returning to paper published in 1974 by deNeufville, Moss and Ovshinsky; this article addressed photo-darkening in $As_2(S, Se)_3$ in a way that anticipated the quantitative definitions for R and L in subsequent publications [7]. This is of historical interest since FSDPs were observed for the first time in each compound and/or alloy studied, and these were associated with a real space distance of $\sim$5.5 A in the MRO regime. It was also noted that the width of this feature in reciprocal (Q) space identified a larger scale of order over which these MRO-regime correlations persisted; this has subsequently been defined as the coherence length, L.

Experimental Results for SiO_2

The position and width of the FSDP in glassy SiO_2 have received considerable attention, and are well-characterized [7, 8, 14]. Based on these references and others as well, $Q_1(\text{Å}^{-1})$ is equal to 1.52 ± 0.03 Å^{-1}, and $\Delta Q_1(\text{Å}^{-1})$ to 0.66 ± 0.03 Å^{-1}. The calculated values of the correlation length, $R = 2\pi/Q_1(\text{Å}^{-1})$, and the coherence length, $L = 2\pi/\Delta Q_1(\text{Å}^{-1})$, are, respectively, $R = 4.13 \pm 0.08$ Å, and $L = 9.95 \pm 0.05$ Å. R gives rise to features in the RDF in a regime associated with rings of bonded atoms;

these are a universal aspect of the CRN description of non-crystalline oxides and chalcogenides which include twofold coordinate atoms [2].

In a continuous random network, CRN, such as SiO_2, the primitive ring size is defined by the number of Si atoms connected through bridging O atoms to form the smallest high symmetry ring structure. This primitive ring is the non-crystalline analog of the primitive unit cell (PUC) in crystalline solids and this provides an important connection between the properties of non-crystalline and nano-crystalline thin films.

It has been first demonstrated in the Bell and Dean model [15, 16], and later by computer generated modeling [17–19], and molecular dynamic simulations as well [8], that the ring size distribution for SiO_2 is dominated by six-member rings with six silicon and six oxygen atoms.

The contributions to the partial structure factor, $S_{ij}^{N}(Q)$ associated with Si–O, O–O and Si–Si pair correlation distances have been determined using classical molecular dynamics simulations as addressed in [8]. Combined with RDFs from the Bell and Dean model [16], and computer modeling [17, 18, 20], these studies identify inter-atomic pair correlations in the regime of 4–5 Å that contribute to the position of FSDP. Figure 3 of [16], is a pair distribution histogram that indicates a (1) a Si–O pair correlation, or third nearest neighbor distance of 4.1 ± 0.5 Å, and (2) an O–O pair correlation, or fourth nearest neighbor distance of 4.5 ± 0.3 Å. These features are evident in the computed and experimental radial distribution function plots for X-ray diffraction in Fig. 4, and neutron diffraction in Fig. 5, also of [16]. As indicated in Fig. 1 of this paper, the 4.1 Å feature is assigned with Si–O third nearest-neighbor distances, and the 4.5 Å feature is assigned to fourth nearest-neighbor O–O distances. Figure 1 is a schematic representation of local cluster that has been used to determine the Si–O–Si bond angle using many-electron ab initio quantum chemistry calculations in [18].

The importance of Si atom d-state symmetries in calculations of the electronic structure of non-crystalline SiO_2 was recognized in [18], published in 2002. These symmetries, coupled with the O 2pπ states play a significant

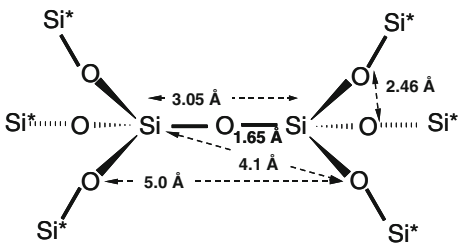

Fig. 1 Two-dimensional top view of the local bonding arrangements in a portion of the primitive high-symmetry six-member ring structure for non-crystalline SiO_2. Selected MRO distances are indicated

role in narrowing the two pair distribution distances identified above. The cluster displayed in Fig. 1 is large enough to include the correlation length, R in the MRO regime. The calculations of [18] demonstrated that Si d-state basis Gaussian functions when included into a many-electron, ab initio calculation play a determinant role in generating a stable minimum for a Si–O–Si bond angle, Θ, that is smaller than the ionic bonding value 180°. In addition these values of Θ, and the bond angle distribution, ΔΘ (1) were different from what had been determined by the X-ray diffraction studies of Mozzi and Warren in [3], but (2) were in excellent agreement with more recent studies that employed a larger range of k or Q [19]. The values obtained by Mozzi and Warren [3] are Θ ∼ 144°, and ΔΘ]FWHM ∼ 30°, whereas the studies in [19] obtained values of Q ∼ 148° and ΔΘ]FWHM ∼ 13–15° that were essentially the same as those calculated in [16]. The Bell and Dean model of [15] in Fig. 2 gave a Si–O–Si bond angle of 152°, and also wide bond angle distribution with a FWHM ∼ 15°. Of particular significance is the significantly narrower Si–O–Si bond angle distribution of the calculations in [18], and the X-ray diffraction studies of [19]. The bond angles and bond distributions of [16, 18, 19] have important implications for the existence of high symmetry six member Si–O rings their importance as the primitive ring structure in both α-quartz and β-quartz, as well as non-crystalline SiO_2.

The identification of the specific MRO regime features obtained from S(Q) rely heavily on the pair correlation functions derived from the Bell and Dean model [16], as well as from computer modeling of the Gaskell group [21] and Tadros et al. [17, 20]. Combined with [16], The Si dπ-O 2pπ-Si dπ symmetry determined overlap and charge transfer from occupied O π-states into otherwise empty Si dπ states, plays the determinant role in forcing the narrowness of this MRO length scale feature. Stated differently, pairs of Si atoms connected through an intervening O atom as in Fig. 1, are strongly correlated by the local symmetries forced on these Si dπ-states. This correlation reflects the even symmetry of the respective Si d-states, and the odd symmetry of the O p-states. In contrast, the coherence length, L, as determined from the FWHM of the FSDP cannot be assigned to a specific inter-atomic repeat distance identified in any of the models addressed above, but instead is an average cluster dimension, in the spirit of the definitions in [6] and [7].

The coherence length, L in SiO_2, as computed from the FWHM of the FSDP, is 9.5 ± 0.5 Å, and this identifies the cluster associated with this length scale. Based on a simple extension of the schematic diagram in Fig. 1, this cluster includes a coupling of at least two, and no more than three symmetric six-member primitive rings. If this cluster is extended well beyond two to three rings in all directions, it

would eventually generate the crystal structure of α-quartz. This helical aspect of this structure gives rise to a right- or left-handed optical rotary property of α-quartz [22]. The helical structure of α-quartz has its parentage in trigonal Se, which is comprised of right or left-handed helical chains with three Se atoms per turn of the helix. The two-atom helix analog is the cinnabar phase of HgS with six atoms/turn, three Hg and three S. α-quartz is the three-atom analog with nine atoms/turn, three Si and six O [22]. Returning to non-crystalline SiO_2, the coupling of two to three-six-member rings is consist with the relative fraction of six member rings, ~50% in the Bell and Dean [16] construction as well as other estimates of the ring fraction.

Moreover, this two to three ring clustered structure is an example of the MRO structures addressed in [7]. With respect the FSDP, Moss and Price noted that "such a diffraction feature thus represents the build up of correlation whose basic period is well beyond the first few neighbor distances"; it therefore in the MRO regime. They also pointed out that: "In fact, the width of this feature (the, FSDP) can be used to estimate a correlation range over which the period in question survives". This incoherent coupling associated with less symmetric five- and seven-member rings than determines the correlation, or coherence range over which this period survives.

Revisiting the CRN in Context of Correlation and Coherence Length Determinations

The pair correlation assignments made for R and L are consistent with the global concept of a CRN, but the length scales for correlation, R, and coherence. L, are quantitatively different that what was proposed originally in [1], and discussed at length [3]. Each of these envisioned the CRN randomness to be associated with the relative widths of bond lengths and bond angles, as in Fig. 2 in the Bell and Dean [16]. Based on this model the Si–O pair correlation has a width <0.05 Å, and the Si–O–Si bond angle displays a 30° width, corresponding to a Si–Si pair correlation width at least two-to-three larger. In these conventional descriptions of the CRN, any dihedral angle correlations, or four-atom correlations, are removed by bond-angle widths.

The identification of the MRO length scales, R and L, also has important implications for the use of semi-empirical bond constraint theory (SE-BCT) for identifying and/or describing ideal glass formers. This theory is a mean-field theory based on average properties that are determined by constraints restricted to SRO bonding arrangements [4, 5, 23]. The identification and interpretation of the two MRO length scales discussed above indicates that this emphasis on SRO is not sufficient for identifying the important nano-scale properties of SiO_2. Indeed MRO is deemed crucial for establishing the unique and technologically important character of non-crystalline SiO_2 over a dimensional scale from 1 to 2 nm thick gate dielectrics to centimeter dimensions for high-quality optically homogeneous components, e.g., lenses.

The FSDP has been observed, and studied in other non-crystalline oxide glasses, e.g., B_2O_3, GeO_2, as well chalcogenide glasses including sulfides, GeS_2 and As_2S_3, and selenides, $GeSe_2$, As_2Se_3 and $SiSe_2$ [6, 7]. The values of R and L have been calculated, and display anion, O, S and Se and cation coordination specific behaviors. For example, the values of the correlation length R, and the coherence length L, have been obtained from the position, and FWHM of the S(Q) FSDP peak for (a) SiO_2: $R = 4.1 \pm 0.2$ Å, and $L = 9.5 \pm 0.5$ Å; (b) B_2O_3: $R = 4.0 \pm 0.2$ Å, and $L = 11 \pm 1$ Å; and (c) $GeSe_2$: $R = 6.3 \pm 0.3$ Å, and $L = 24 \pm 4$ Å.

It has been noted previously elsewhere [7, 13], that quantitative differences between the position of the FSDPs in SiO_2 and $GeSe_2$ can be correlated directly with differences between the respective (1) Si–O and Ge–Se bond-lengths, 1.65 and 2.39 Å, and (2) Si–Si and Ge–Ge next neighbor features as determined by the respective Si–O–Si and Ge–Se–Ge bond angles, ~148° and ~105°. This was addressed in [1] and [24], where it was shown that the products of nearest neighbor bond length (in Å) and positions of the FSDP (Q(Å^{-1}) are approximately the same, ~2.5 ± 0.4 for the oxide and chalcogenide glasses [1, 24]. Based on this scaling, the value R for $GeSe_2$ ($x = 0.33$), is estimated to be 6.2 ± 0.2 Å, compared with the averaged experimental value of $R = 6.30 \pm 0.07$ Å.

This values of Q_1(Å^{-1}) show interesting correlations with the nature of the CRNs. For the three oxide glasses in Table 1 Q_1(Å^{-1}) ~ 1.55 ± 0.03, and is independent of the network coordination, i.e., 3–2 for B_2O_3 and 4–2 SiO_2 and GeO_2. In contrast, the value of Q_1(Å^{-1}) decreases to ~1.05 for 4–2 selenides, and then increases to ~1.25 for the 3–2 chalcogenides. This indicates a longer correlation length in the 3–2 alloys that is presumed to be associated with repulsions between lone pairs on As, and either the Se or S atoms of the particular alloy for the 3–2 chalcogenides.

It is significant to note that the scaling relationship based on SRO, breaks down for the coherence length L for $GeSe_2$. The scaled ratio for L is estimated to be 15 Å compared with the higher average experimental value of $L = 24 \pm 4$ Å [11, 25]. The comparisons based on scaling are consistent with R being determined by the extension of a local pair correlation determined by the ring structures in the SiO_2 and $GeSe_2$ CRNs. The microscopic basis for L in SiO_2, and B_2O_3 as well, is determined by characteristic inter-ring bonding arrangements with a cluster size that related to coupling of two, two or three rings, respectively. These determine the

Table 1 Comparisons and scaling for R [1]

Glass	Q_1 (Å^{-1})	R (Å)	r_1 (Å)	r_1Q_1
SiO_2	1.55	4.1	1.61	2.48
GeO_2	1.55	4.1	1.74	2.70
B_2O_3	1.57	4.0	1.36	2.14
$SiSe_2$	1.02	6.2	2.30	2.35
GeS_2	1.00	6.3	2.37	2.37
GeS_2	1.04	6.0	2.22	2.30
As_2S_2	1.27	4.9	2.28	3.10
As_2S_2	1.26	5.0	2.44	2.87

r_1 = bond length

period of the cluster repetition, and the encapsulation of these more symmetric rings by less symmetric rings of bonded atoms; i.e., five- and seven-member rings in SiO_2. The inter-ring coupling in SiO_2 is direct result of the softness of the Si–O–Si bonding force constant in SiO_2 [4, 5]. For the case of the $GeSe_2$ CRN because of the smaller Ge–Se–Ge bond angle and repulsive effects between the Se lone pair electrons and the bonding electrons localized in the more covalent Ge–Se bonds, the coherence length is not attributed to rings of bonded atoms, but rather to a hard soft cluster mixture. The hard soft structure in GeSe alloys is determined by compositionally dependent constraints imposed by local bonding, e.g., locally rigid groups with Ge atoms separated by one bridging Se atom, Ge–Se–Se, and locally compliant groups associated with two bridging Se atoms, Ge–Se–Se–Ge [23]. Similar considerations apply to the period of the hard-component of a hard-soft structure that have been proposed as the driving force for glass formation, and the associated low densities of defect and defect precursors which are associated with either broken and strained-bonds, respectively. The criterion is SiO_2 and B_2O_3 is determined by a nano-structures that includes a multiplicity of different ring sizes, whereas the criterion is a volume percolation threshold that applies in chalcogenides glasses, and is consistent with locally rigid, and locally compliant groups been phase-separated into hard-soft mixtures [26]. The same considerations apply in As-chalcogenides, and for the compound As_2Se_3 and $GeSe_2$ compositions that include local small discrete molecules that add compliance to the otherwise locally rigid CNRs that includes As–Se–As and Ge–Se–Ge bonding, respectively [23].

The conclusion is that SE-BCT, even with local modifications for symmetry-associated broken bending constraints, and additional constraints due to lone pair and terminal atom repulsions [23], has limited value in accounting the elimination of macroscopic strain reduction for technology applications. This property depends on MRO, as embodied in hard-soft mixtures, and/or percolation of short-range order ground that exceeds a volume percolation threshold [23, 27].

Nano-crystalline and Nano-crystalline/Non-crystalline Alloys

Extension of the MRO concepts of the previous sections from CRNS to nano-crystalline and nano-crystalline/non-crystalline composites of technological importance is addressed in this section. One way to formulate this issue is to determine conditions that promote hard-soft mixtures in materials that are (1) chemically homogeneous, but inhomogeneous on a nano-meter length scale, or (2) both chemically inhomogeneous and phase-separated. The first of these is addressed in homogeneous HfO_2 thin films, and the second for phase separated Hf silicates, as well as other phase separated materials in which SiO_2 in a chemical constituent [28].

Nano-grain HfO_2 Films

The nano-grain morphology of deposited and subsequently high temperature, >700°C, annealed HfO_2 thin films is typically a mixture of monoclinic (m-) and tetragonal (t-) grains differentiated by Hf 5d features in combination with O 2p π states that comprise local symmetry adapted linear combinations (SALCs) of atomic states into molecular orbitals (MO) [28, 29]. These MOs are essentially one-electron states, in contrast to occupied Hf states that must by treated in a many-electron theory [30]. Of particular importance are the π-bonded MOs that contribute to the lowest conduction band features in O K edge XAS spectra [28, 29]. Figure 2 indicates differences in these band edge features for nano-grain t-HfO_2 and m-HfO_2 thin films in which the grain-morphology has been controlled by interfacial bonding. The t-HfO_2 films display a single asymmetric band edge feature, whereas m-HfO_2 films display two band edge features. Figure 3 is for films that have with a mixed t-/m- nano-grain morphology, and a thickness that is increased from 2 to 3 nm, and then to 4 nm. Based of features in these spectra, and 2nd derivative spectra as well, the 2 nm film displays neither a t-, nor a m-nano-grain morphology, while the thicker films display a doublet structure indicative of a mixed nano-grain morphology.

The band edge 5d E_g splittings in Figs. 2 and 3 indicate a cooperative Jahn–Teller (J–T) distortion [28]. The theoretical model in [31] indicates that an electronic unit cell comprised of seven PUCs, each ~0.5 to 0.55 nm is necessary for a cooperative J–T effect, and this requires a nano-grain dimensions of ~3 to 3.5 nm. This indicates a dimensional constraint in the 2 nm thick film. This film is simply too thin to support a high concentration of randomly oriented nano-grains with an electronic unit cell large enough to support a J–T distortion. These 2 nm films are generally characterized as X-ray amorphous. As-deposited 3 and 4 nm thick films also display no J–T, but when

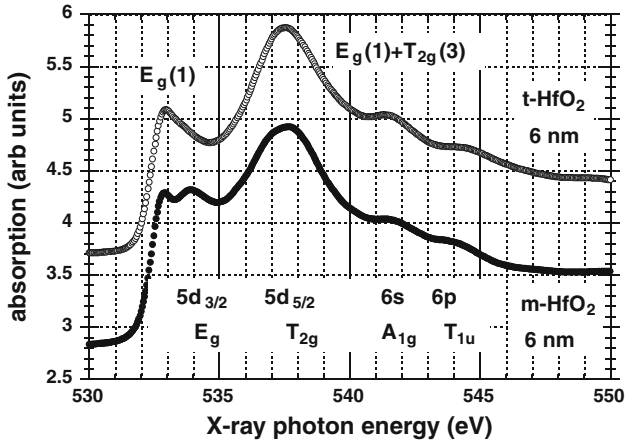

Fig. 2 O K edge for t-HfO_2 and m-HfO_2 indicating differences in these band edge features

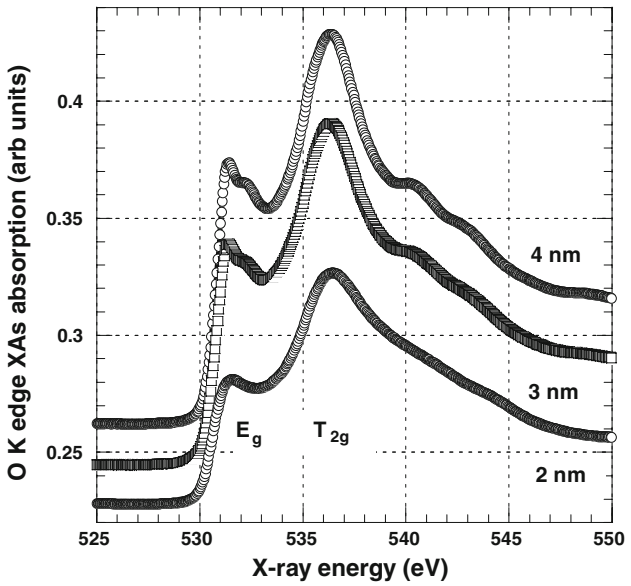

Fig. 3 O K edge for mixed phase 900°C annealed t-/m-HfO_2 films as a function of film thickness

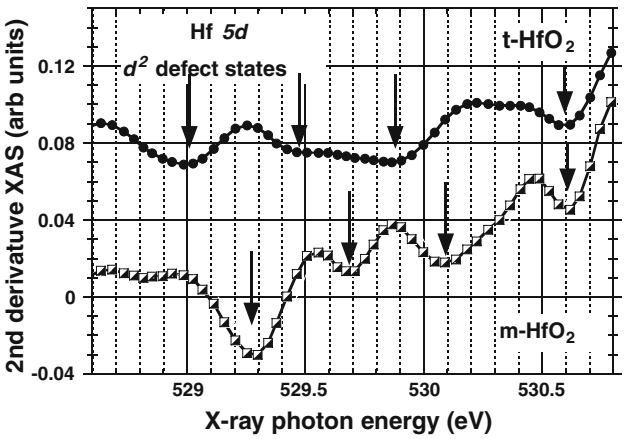

Fig. 4 Second derivative O K pre-edge for t-HfO_2 and m-HfO_2. The features in these films are associated with band edge vacancy defects

subjected to the same 900°C anneal as the 2 nm thick film, the dimensional constraint is relaxed and J–T distortions are stabilized and are observed in O K edge XAS.

These differences in nano-scale morphology identify several scales of MRO for HfO_2, as well as other TM d^0 oxides, TiO_2 and ZrO_2. The first is the PUC $\sim$ 0.5 to 0.55 nm, and the second and third are for coupling of unit cells. The first coupling is manifest in 1.5–2.0 nm grains that are analogues of the SiO_2 clusters comprised of 2–3 symmetric six-member rings. The second length scale is 3–3.5 nm and is sufficient to promote J–T distortion which persist in thicker annealed film and bulk crystals as well. The PUC of HfO_2 then plays the same role as the symmetric or regular six-member ring of non-crystalline SiO_2 and in crystalline a-quartz.

Differences in nano-grain order have a profound effect on intrinsic bonding defects in HfO_2. In films thicker than 3 nm they contribute to high densities of vacancy defects ($\sim 10^{12}$ cm^{-2}, or equivalently 10^{18} cm^{-3}), clustered on internal grain boundaries of nano-grains large enough to display J–T term splittings [28]. These are indicated in Fig. 4.

Nano-grain HfO_2 in the MRO size regime of 1.5–2 nm can also formed in phase-separated Hf silicates $(HfO_2)_x(SiO_2)_{1-x}$, alloys in two narrow compositional regimes: $0.15 < x < 0.3$, and $0.75 < x < 0.85$. For the lower x-regime, the phase separation of an as-deposited homogeneous silicate yields a compliant hard-soft structure. This is comprised of X-ray amorphous nano-grains with <3 nm dimensions that are encapsulated by non-crystalline SiO_2. For the higher x-regime. The phase separated silicates include X-ray amorphous nano-grains <3 nm in size, whose growth is frustrated by a random incorporation of 2 nm clusters of compliant non-crystalline SiO_2. The concentration of these 2 nm clusters exceeds a volume percolation threshold accounting for the frustration of larger nano-grain growth [27].

Each of these phase-separated silicate regimes exhibits low densities of defects and defect precursors. However, these diphasic silicates have not studied with respect to radiation stressing, so it would be ill-advised and inappropriate to call then SiO_2-look-alikes, a label that has been attached to the homogeneous Hf Si oxynitride alloys in the next sub-section based on radiation stressing [32].

Homogeneous Hf Si Oxynitride Alloys

There is a unique composition $(HfO_2)_{0.3}(SiO_2)_{0.3}(Si_3N_4)_{0.4}$ (concentrations $\pm$ 0.025) hereafter $HfSiON_{334}$, which is stable to annealing temperatures >1,000°C, and whose electrical response after X-ray and γ-ray stressing is

essentially the same as SiO_2 [32].This similarity is with respect to (1) the linear dependence on dosing, (2) the sign of the fixed charge, always positive, and (3) the magnitude of the defect generation. The unique properties are attributed to a fourfold coordinated Hf substitute onto 16.7% of the possible fourfold coordinated Si bonding sites. This concentration is at the percolation threshold for connectivity of compliant local bonding arrangements [27]. Larger concentrations of (Si_3N_4) for the same or different combinations of HfO_2 and SiO_2 bonding leads to chemical phase separation with loss of bonded N, and therefore qualitatively different thin films.

Other Diphasic Materials with 20% SiO_2

There are at least two other diphasic materials with a dimensionally stabilized symmetric nano-crystalline phase, and a 20% compliant non-crystalline phase, 2 nm clusters of SiO_2. This includes a 20% mixture of non-crystalline SiO_2 with (1) nano-crystalline zincblende-structured ZnS grains, or (2) a fine nano-grain ceramic as in Corning cookware [33]. In each of these thin materials, TEM imaging indicates that the 20% SiO_2 is distributed uniformly in compliant clusters with an average size of $\sim$2–3 nm. These encapsulated nanoclusters reduce macroscopic strain, but equally important suppress the formation of more asymmetric crystal structures, e.g., wurtzite ZnS, which would lead to anisotropic optical properties, and make these films in unusable for use as protective layers in optical memory stacks for digital video disks (DVD) for information storage and retrieval. In the second application, the SiO_2 makes these ceramics macroscopically strain free, and capable on being moved from the "oven to the refrigerator" without cracking [33].

$(Si_3N_4)_x(SiO_2)_{1-x}$ Gate Dielectrics

Si oxynitride pseudo-binary alloys $(Si_3N_4)_x(SiO_2)_{1-x}$, have emerged in the late 1990s as replacement dielectrics [34]. These alloys have been used with small and high concentrations of Si_3N_4 with different objectives. At low concentration levels <5% Si_3N_4, for blocking Boron transported from B-doped poly-Si gate dielectrics [24], and at significantly higher concentrations, $\sim$50 to 60% Si_3N_4, as required for a significant increase in the dielectric constant from $\sim$3.9 to $\sim$5.4 to 5.8 [35].

The mid-gap interface state density, D_{it}, and the flat-band voltage V_{fb} were obtained from a conventional C–V analysis of metal–oxide–semiconductor capacitors on p-type Si substrates with $\sim 10^{17}$ cm^{-3} doping, *p*-MOSCAPs, with Al gate metal layers deposited after a post metal anneal in forming gas. Both D_{it} and and V_{fb} display qualitatively similar behavior as function of x for both as-deposited and Si-dielectric layers annealed at 900°C in Ar for 1 min [34]. The annealed dielectrics are processed at temperatures that validate comparisons with *p*-MOSCAPs with thermally grown SiO_2 and similarly processed Al gates. D_{it} decreases from $\sim 10^{11}$ cm^{-2} eV^{-1} for Si_3N_4 ($x = 1$), to $\sim 10^{10}$ cm^{-2} eV^{-1} for $x \sim 0.7$ to a value comparable to state of the art SiO_2 MOSCAPs. The value of D_{it} is relatively constant, $1.1 \pm 0.2 \times 10^{-10}$ cm^{-2} eV^{-1}, for values of x from 0.65 to 0.0 (SiO_2). In a complementary manner, V_{fb} increases from -1.3 eV for Si_3N_4 ($x = 1$), to -0.9 eV at $x \sim 0.7$, and then remains relatively constant, -0.8 ± 0.1 eV for values of x from 0.65 to 0.0 (SiO_2). The values of D_{it} and V_{fb} are comparable to those for thermally grown SiO_2, and therefore have been the basis for use of these Si oxynitrides in commercial devices [34].

The electrical measurements are consistent with significant decreases in macroscopic strain for Si oxnitride alloys with SiO_2 concentrations exceeding about 35% or $x = 0.65$. This suggests a hard-soft mechanism in this regime similar to that in Hf silicates. At concentrations <0.35, i.e., $SiO_2 = 65\%$, the roles of the hard and soft components are assumed to be reversed. However, strain reduction over such an extensive composition regime suggests a more complicated nano-scale structure that has a mixed hard-soft character over a significant composition region, The proposed mixed phase is comprised of equal concentrations of Si_3N_4 encapsulating SiO_2 at high Si_3N_4 concentrations, and an inverted hard-soft character with SiO_2 encapsulating Si_3N_4 at lower Si_3N_4 concentrations. If this is indeed the case, it represents a rather interesting example of a double percolation process [26, 36].

Summary and Conclusions

This will be displayed in a bulleted format.

1. The spectral position of the FSDP for glasses, and its FWHM are associated with real space distances as obtained from the structure factor S(Q) derived from X-ray or neutron diffraction\are in the MRO regime. The first length scale has been designated as a correlation length, $R = 2\pi/Q_1(Å^{-1})$, and the second length scale has been designated as a coherence length, $L = 2\pi/\Delta Q_1(Å^{-1})$ where $Q_1(Å^{-1})$ and $\Delta Q_1(Å^{-1})$ are, respectively, the position and FWHM of S(Q).
2. The values of the correlation length R, and the coherence length L, obtained in this way are for: (a) SiO_2: $R = 4.1 \pm 0.2$ Å, and $L = 9.5 \pm 0.5$ Å; (b) B_2O_3: $R = 4.0 \pm 0.2$ Å, and $L = 11 \pm 1$ Å; and (c) $GeSe_2$: $R = 6.3 \pm 0.3$ Å, and $L = 24 \pm 4$ Å.
3. Based on molecular dynamics calculations and modeling, the values of R correspond to third

neighbor Si–O, and associated with segments of six-member rings in SiO_2. The larger value of R in $GeSe_2$ is consistent with scaling based on Ge–Se bond lengths and therefore has a similar origin.

4. Based on molecular dynamics calculations and modeling, the coherence length features are not a direct result of inter-atomic pair correlations. This is supported by the analysis of X-ray diffraction data as well, where the coherence length is determined by the width of the FSDP rather than by an additional peak in S(Q).
5. The ring clusters contributing to the coherence lengths for SiO_2 are comprised of two, or at most three symmetric six-member rings, that are stabilized by back donation of electrons from occupied 2p π states on O atoms to empty π orbitals on the Si atoms. These rings are encapsulated by more compliant structures with lower symmetry irregular five- and seven-member rings to form a compliant hard-soft system.
6. The coherence length in Ge_xSe_{1-x} alloys is different in Se-rich and Ge-rich composition regimes, and is significantly larger in each of these regimes than at the compound composition, $GeSe_2$ which they bracket. It is determined in each alloy regime, and at the compound composition by minimization of macroscopic strain by a chemical bonding self-organization as in which site percolation dominates. There is a compliant alloy regime which extends from $x = 0.2$ to 0.26 in which locally compliant bonding arrangements, Ge–Se–Se–Ge, completely encapsulate a more rigid cluster comprised of locally rigid Ge–Se–Ge bonding. For compositions greater than $x = 0.26$ and extending to $x = 0.4$, macroscopic compliance results form a diphasic mixture which includes small molecules with Ge–Se, and Ge–Ge bonding.
7. The hard-soft mix in non-crystalline SiO_2 with a length scale of at most 1 nm establishes the unique properties of gate dielectrics >1–1.5 nm thick, and for cm glasses with cm-dimensions as well.
8. There is an analog between the properties of nano-crystalline HfO_2, and phase separated HfO_2-SiO_2 silicate alloys, ZnS-SiO_2 alloys and ceramic-SiO_2 alloys that establishes their unique properties in device applications as diverse as gate dielectrics for aggressively scaled dielectrics, protective layers for stacks in with rewritable optical information storage, and for temperature compliance in ceramic cookware.
9. p-MOSCAPs with Si oxynitride pseudo-binary alloys $(Si_3N_4)_x(SiO_2)_{1-x}$, gate dielectrics display an defect densities for interface trapping, D_{it}, and fixed positive charge that determines the flat-band voltage, V_{fb}, comparable to those of thermally grown SiO_2 dielectrics for a range of concentrations extending for $\sim$70%, $x = 0.7$, Si_3N_4 to SiO_2. The electrical measurements are consistent with significant decreases in macroscopic strain, suggesting a hard-soft mechanism in this regime similar to that in Hf silicates. However, strain reduction over such an extensive composition regime suggests a more complicated nano-scale structure that has a mixed hard-soft character over a significant composition region, The proposed mixed phase is comprised of equal concentrations of Si_3N_4 encapsulating SiO_2 at high Si_3N_4 concentrations, and an inverted hard-soft character with SiO_2 encapsulating Si_3N_4 at lower Si_3N_4 concentrations. If this is indeed the case, it represents a rather interesting example of a double percolation process.
10. The properties of the films and bulk materials identified above are underpinned by the real-space correlation and coherence lengths, R and L, obtained from analysis of the SiO_2 structure factor derived from X-ray or neutron diffraction. The real space interpretation relies of the application of many-electron theory to the structural, optical and defect properties on non-crystalline SiO_2.

Acknowledgments One of the authors (G. L.) acknowledges support from the AFOSR, SRC, DTRA and NSF.

References

1. W.H. Zachariasen, J. Am. Chem. Soc. **54**, 3841 (1932)
2. R. Zallen, *The physics of amorphous solids* (Wiley-Interscience, New York, 1983)
3. L. Mozzi, B.E. Warren, J. Appl. Crystallogr. **2**, 164 (1969)
4. J.C. Phillips, J. Non-Cryst. Solids **34**, 153 (1979)
5. J.C. Phillips, J. Non-Cryst. Solids **43**, 37 (1981)
6. J. DeNeufville et al., J. Non-Cryst. Solids **13**, 191 (1974)
7. S.C. Moss, D.L. Price, in *Physics of disordered materials*, ed. by D. Adler, H. Fritzsche, S.R. Ovshinsky (Plenum, New York, 1985), p. 77
8. J. Du, L.R. Corrales, Phys. Rev. B 72, 092201 (2005), and references therein
9. T. Uchino et al., Phys. Rev. B **71**, 014202 (2005)
10. S.R. Elliott, Phys. Rev. Lett. **67**, 711 (1991)
11. N.R. Rao et al., J. Non-Cryst. Solids **240**, 221 (1998)
12. C. Massobrio, A. Pasquarello, J. Chem. Phys. **114**, 7976 (2001)
13. D.L. Price et al., J. Phys. Condens. Matter **1**, 1005 (1989)
14. S. Sussman et al., Phys. Rev. B **43**, 1194 (1991)
15. R.J. Bell, P. Dean, Nature **212**, 1354 (1966)

16. R.J. Bell, P. Dean, Philos. Mag. **15**, 1381 (1972)
17. A. Tadros, M.A. Klenin, G. Lucovsky, J. Non-Cryst. Solids **75**, 407 (1985)
18. J.L. Whitten et al., J. Vac. Sci. Technol. B **20**, 1710 (2002)
19. J. Neufeind, K.-D. Liss, Bur. Bunsen. Phys. Chem. **100**, 1341 (1996)
20. A. Tadros, M.A. Klenin, G. Lucovsky, J. Non-Cryst. Solids **64**, 215 (1984)
21. K.M. Evans, P.H. Gaskell, C.M.M. Nex, in *The structure of non-crystalline materials 1982*, ed. by P.H. Gaskell, J.M. Parker, E.A. Davis (Talyor and Francis, London, 1983), p. 426
22. R. Zallen et al., Phys. Rev. B **1**, 4058 (1970)
23. G. Lucovsky, J.C. Phillips, J. Phys. Condens. Mater. **19**, 455218 (2007)
24. Y. Wu et al., J. Vac. Technol. B **17**, 3017 (1999)
25. M.T.M. Shatnawi et al., Phys. Rev. B **77**, 094134 (2008)
26. J.C. Phillips, J. Phys. Condens. Mater. **19**, 455213 (2007)
27. H. Scher, R. Zallen, J. Chem. Phys. **53**, 3759 (1970)
28. G. Lucovsky, et al., Jpn. J. Appl. Phys. 46, 1899 (2007), and references therein
29. F.A. Cotton, *Chemical applications of group theory*, 2nd edn. (Wiley-Interscience, New York, 1953)
30. F. de Grott, A. Kotani, *Core level spectroscopy of solids* (CRC, Boca Ratan, 2008). Chapters 2, 3 and 4
31. I.B. Bersuker, J. Comput. Chem. **18**, 260 (1997)
32. D.K. Chen, et al., IEEE Trans. Nucl. Sci. 54, 1931 (2007), and references therein
33. G. Lucovsky, Phys. Status Solid A **206**, 915 (2009)
34. S.V. Hattangady et al., J. Vac. Technol. A **14**, 3017 (1996)
35. Y. Wu et al., IEEE Trans. Electron. Devices **47**, 1361 (2000)
36. G. Lucovsky, J.C. Phillips, J. Phys. Condens. Mater. **19**, 455218 (2007)